


## Article

# Improving the Catalytic CO<sub>2</sub> Reduction on Cs<sub>2</sub>AgBiBr<sub>6</sub> by Halide Defect Engineering: A DFT Study

Pengfei Chen <sup>1,2,†</sup>, Yiao Huang <sup>1,2,†</sup> , Zuhao Shi <sup>1,2,3</sup>, Xingzhu Chen <sup>1,3</sup> and Neng Li <sup>1,3,4,\*</sup> 

<sup>1</sup> State Key Laboratory of Silicate Materials for Architectures, Wuhan University of Technology, Wuhan 430070, China; pengfeichen\_whut@163.com (P.C.); hyahya0211@163.com (Y.H.); zuhao110317@163.com (Z.S.); chen.xz0913@gmail.com (X.C.)

<sup>2</sup> Center of Innovation and Entrepreneurship, Wuhan University of Technology, Wuhan 430070, China

<sup>3</sup> Shenzhen Research Institute, Wuhan University of Technology, Shenzhen 518000, China

<sup>4</sup> State Center for International Cooperation on Designer Low-Carbon & Environmental Materials (CDLCEM), School of Materials Science and Engineering, Zhengzhou University, Zhengzhou 450001, China

\* Correspondence: lineng@whut.edu.cn

† These authors contribute equally to this work.

**Abstract:** Pb-free double halide perovskites have drawn immense attention in the potential photocatalytic application, due to the regulatable bandgap energy and nontoxicity. Herein, we first present a study for CO<sub>2</sub> conversion on Pb-free halide perovskite Cs<sub>2</sub>AgBiBr<sub>6</sub> under state-of-the-art first-principles calculation with dispersion correction. Compared with the previous CsPbBr<sub>3</sub>, the cell parameter of Cs<sub>2</sub>AgBiBr<sub>6</sub> underwent only a small decrease of 3.69%. By investigating the adsorption of CO, CO<sub>2</sub>, NO, NO<sub>2</sub>, and catalytic reduction of CO<sub>2</sub>, we found Cs<sub>2</sub>AgBiBr<sub>6</sub> exhibits modest adsorption ability and unsatisfied potential determining step energy of 2.68 eV in catalysis. We adopted defect engineering (Cl doping, I doping and Br-vacancy) to regulate the adsorption and CO<sub>2</sub> reduction behavior. It is found that CO<sub>2</sub> molecule can be chemically and preferably adsorbed on Br-vacancy doped Cs<sub>2</sub>AgBiBr<sub>6</sub> with a negative adsorption energy of −1.16 eV. Studying the CO<sub>2</sub> reduction paths on pure and defect modified Cs<sub>2</sub>AgBiBr<sub>6</sub>, Br-vacancy is proved to play a critical role in decreasing the potential determining step energy to 1.25 eV. Finally, we probe into the electronic properties and demonstrate Br-vacancy will not obviously promote the process of catalysis deactivation, as there is no formation of deep-level electronic states acting as carrier recombination center. Our findings reveal the process of gas adsorption and CO<sub>2</sub> reduction on novel Pb-free Cs<sub>2</sub>AgBiBr<sub>6</sub>, and propose a potential strategy to improve the efficiency of catalytic CO<sub>2</sub> conversion towards practical implementation.

**Keywords:** halide perovskite; CO<sub>2</sub> catalytic reduction; defect engineering; computational research



**Citation:** Chen, P.; Huang, Y.; Shi, Z.; Chen, X.; Li, N. Improving the Catalytic CO<sub>2</sub> Reduction on Cs<sub>2</sub>AgBiBr<sub>6</sub> by Halide Defect Engineering: A DFT Study. *Materials* **2021**, *14*, 2469. <https://doi.org/10.3390/ma14102469>

Academic Editor: Ivano E. Castelli

Received: 9 April 2021

Accepted: 7 May 2021

Published: 11 May 2021

**Publisher's Note:** MDPI stays neutral with regard to jurisdictional claims in published maps and institutional affiliations.



**Copyright:** © 2021 by the authors. Licensee MDPI, Basel, Switzerland. This article is an open access article distributed under the terms and conditions of the Creative Commons Attribution (CC BY) license (<https://creativecommons.org/licenses/by/4.0/>).

## 1. Introduction

Many environmental problems such as global warming [1–4], water pollution, and natural resource depletion have spurred numerous researchers to devote concerted efforts to realizing the high-efficiency production of clean, reliable, renewable energy. Among all the proposed strategies, catalytic conversion of carbon dioxide (CO<sub>2</sub>), of which the released amount has far exceeded it that our ecosystem can handle, has become one of the hottest research spheres. In this regard, photo(electro)catalytic hydrogenate of CO<sub>2</sub> in hydrocarbon-based “green fuels” is regarded as state-of-the-art technology. It will contribute to less reliance on fossil fuels with CO<sub>2</sub> reduction production, serving as a substitute high-energy-density fuel. It will also introduce a carbon resource in the carbon-cycling which is crucial in the sustainable development of the earth [5,6]. Thus far, extensive works have witnessed great interest in semiconductors such as TiO<sub>2</sub> [7–10], Cu<sub>2</sub>O [11,12], CdS [13,14] and g-C<sub>3</sub>N<sub>4</sub> [15,16], with lots of experimental investigations focusing on promoting the migration rate of induced charges. However, more studies are required to

uncover novel and effective ideas, properties, and aspects of the CO<sub>2</sub> conversion catalysts to further advance the present state of knowledge and reaction performance to the next level.

From the view of atomic and electronic points, CO<sub>2</sub> reduction can be mainly divided into two steps: forming a strong interaction between the gas molecules and the catalysts, followed by reduction reaction in the existing H<sup>+</sup>/e<sup>-</sup> pairs. Determined by varied catalysts and reaction environment (i.e., carbonate solution, CO<sub>2</sub> mixed with H<sub>2</sub>O vapor, pure CO<sub>2</sub> gas, and so on), two to eight even numbers of the pairs will be utilized in the whole reaction leading to different final products such as CO, HCOOH, H<sub>2</sub>CO, CH<sub>3</sub>OH, and CH<sub>4</sub>. Nevertheless, few works give a deep insight into the relationship between CO<sub>2</sub> molecular with catalysts, as the CO<sub>2</sub> conversion efficiency highly depends on the surface reaction [17–20]. The successive physicochemical adsorption of the small gas molecular on to the catalyst surface guarantees effective catalysis. However, CO<sub>2</sub> is not preferred to be fixed, and methods like additional energy, pressure, and temperature are often adopted to confirm the process of fixation. After that, the CO<sub>2</sub> reduction encounters another challenge of first step hydrogenation: CO<sub>2</sub> + e<sup>-</sup> → CO<sup>2-</sup> which needs a critical amount of energy to climb over a reaction barrier as large as -1.90 V vs. NHE (normal hydrogen electrode, the detail is displayed in the Electronic Supplementary Material (ESI)) in the electrochemical study. Consequently, there is a pressing need and huge quest to provide novel kinds of next-generation semiconductors with a followed optimized method to overcome the bottlenecks and cover the in-depth study of reaction mechanism to give a theoretical foundation for future researches.

Following the guidance of finding a more promising semiconductor, a great number of researches have paid attention to conventional inorganic perovskites ABO<sub>3</sub> (i.e., CaTiO<sub>3</sub>, SrTiO<sub>3</sub>), which possess remarkable structural flexibility and stability with a myriad of studies [21–25] reporting the unique catalytic performance. Nonetheless, the large bandgap, high carriers recombination rate, small surface area, and unsatisfactory selectivity of CO<sub>2</sub> reduction are still the challenges as a prominent catalyst for ABO<sub>3</sub>. As for the new kind of halide Pb-based perovskites ABX<sub>3</sub> (i.e., CH<sub>3</sub>CH<sub>2</sub>PbI<sub>3</sub>, CsPbBr<sub>3</sub>), the toxicity of Pb<sup>2+</sup> is the major bottleneck for the experimental synthesis [26–32].

Recently, novel Pb-free double halide perovskites A<sub>2</sub>BB'X<sub>6</sub> have witnessed rapid advances in the past two years as a new star of catalyst. Due to the diverse collocation of atoms on the B/B' sites, the intrinsic properties can be easily modulated. Moreover, the double perovskite structure can effectively tackle the toxicity of traditional lead halide perovskites [33]. The most typical double perovskite Cs<sub>2</sub>AgBiBr<sub>6</sub> [34] shows a lack of toxicity compared with CsPbBr<sub>3</sub>, and its nanocrystal has demonstrated great potential as appealing candidates for the advanced photo(electro)catalytic applications [35,36].

Up to now, four types of double perovskites have been synthesized with different kinds of B and B' cations (i.e., B = Li<sup>+</sup>, Na<sup>+</sup>, K<sup>+</sup>, Rb<sup>+</sup>, etc. and B' = In<sup>3+</sup>, Tl<sup>3+</sup>, Bi<sup>3+</sup>, Sb<sup>3+</sup>, etc.), among which type A, B, and C all adopt the strategy of substituting Pb<sup>2+</sup> by monovalent and trivalent ions, while type D reveals B cation vacancy and tetravalent B' cation. Figure 1 has concluded nearly all the construction routes of double perovskites, synthesis compositions, and the electronic properties followed by potential applications. Among all the inorganic halide Pb-free perovskites, Cs<sub>2</sub>AgBiBr<sub>6</sub> double perovskite exhibits unique semiconducting properties equipped with suitable band edges for CO<sub>2</sub> reduction, high stability and nontoxicity, which can be exploited for various industrial and artificial applications in catalytic CO<sub>2</sub> conversion [33,37,38]. However, there is little research reported to investigate the CO<sub>2</sub> capture and conversion on the Pb-free double halide perovskites. Meanwhile, almost all the mechanism on CO<sub>2</sub> conversion are established on the hypothesis that CO<sub>2</sub> is the only existing gas in the reaction environmental. The question remains of whether this material be applied to the real reaction environment. Therefore, probing into the structural and electronic properties of the catalysts and using the atom-scale regulation strategy to optimize the catalytic activity is imperative. Herein, using state-of-the-art DFT calculations with dispersion corrections, Cs<sub>2</sub>AgBiBr<sub>6</sub> is comprehensively evaluated as the potential

photocatalyst for CO<sub>2</sub> reduction. The capture performance of CO<sub>2</sub> in the exhaust is examined and indicates the priority of the adsorption of CO<sub>2</sub>. In addition, the detailed CO<sub>2</sub> conversion mechanism on the pure Cs<sub>2</sub>AgBiBr<sub>6</sub> is explored, and halide defect engineering strategies (Cl, I, Br-vacancy doping) are proved to promote the process of CO<sub>2</sub> reduction at different degrees. Finally, we probe into the electronic properties and demonstrate Br-vacancy will not obviously accelerate the deactivation of catalysis, as there is no formation of deep-level electronic states acting as carrier recombination center. This work reveals the process of gas adsorption and CO<sub>2</sub> reduction on novel Pb-free Cs<sub>2</sub>AgBiBr<sub>6</sub>, and then propose a potential strategy to improve the efficiency of catalytic CO<sub>2</sub> conversion towards practical implementation.

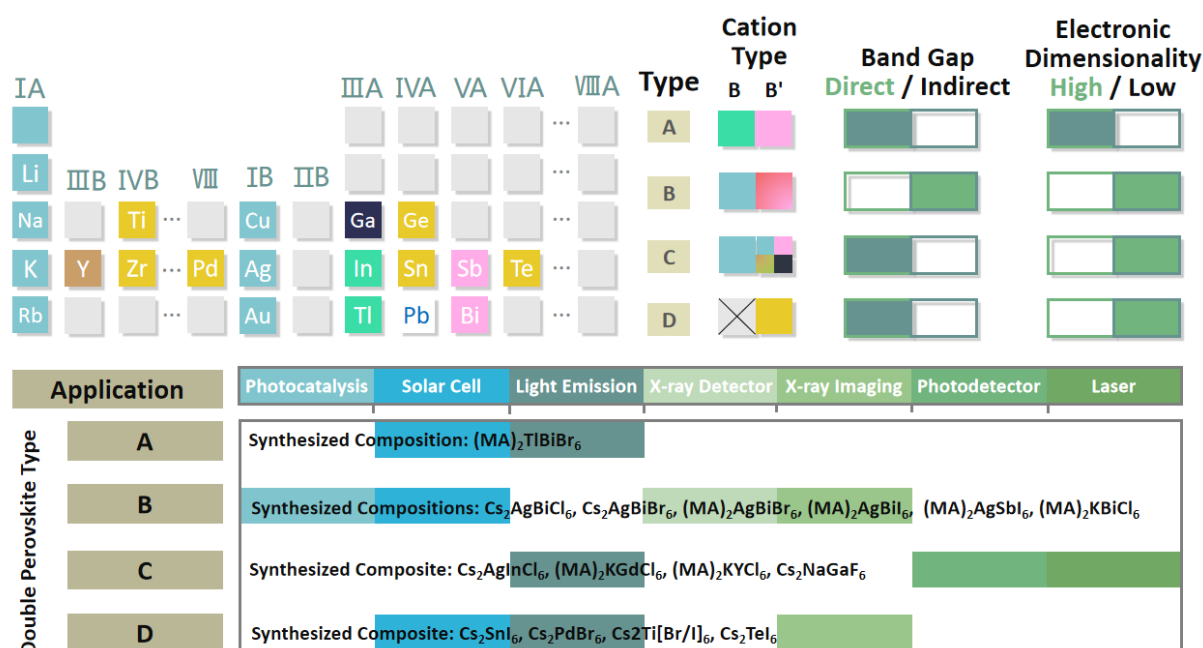


**Figure 1.** Design strategies of lead-free double perovskites by replacing Pb<sup>2+</sup> with B and B' cations, synthesis compositions, and the relationship between their electronic properties and potential applications. The concept “Electronic Dimensionality” is used to describe the ability of carriers transporting in different directions [39,40]. Reproduced with permission from [36].

## 2. Computational Method

Our first-principles calculations were performed using the plane-wave pseudopotential approach under the density functional theory (DFT). And the operations were conducted within the Vienna Ab-initio Simulation Package (VASP) (5.3.5, Neng Li group, Wuhan University of Technology, Wuhan, China) code [41–43]. The generalized gradient approximation (GGA) was adopted to describe the exchange correlation functional in the form of Perdew-Burke-Ernzerhof (PBE) [44]. To more precisely describe the Van der Waals force between the substrate of the perovskite and the gas molecular, we employed the DFT-D3 empirical correction of Grimme [44]. During the optimization process, the cut-off energy was set as 250 eV for electron plane wave basis, and the convergence criteria of residual energy and force for each atom were set to 10<sup>−4</sup> eV and 0.05 eV/Å. A 3 × 3 × 1 Monkhorst-Pack k-point was adopted in geometry optimization. In regard of studying the gas adsorption and CO<sub>2</sub> conversion performance, a vacuum layer of 15 Å was established in the z-direction to construct the surface model. In calculating the band structure, Heyd-Scuseria-Ernzerhof (HSE) hybrid method was employed with the exact Fock exchange set to be 25%. Spin-orbit coupling (SOC) was considered, which was significant in the presence of Bi.

The catalytic reduction of CO<sub>2</sub> can be divided into proton-coupled electron transfer (PCET) steps one by one, with the possible products of CO, HCOOH, H<sub>2</sub>CO, CH<sub>3</sub>OH, and CH<sub>4</sub>. In each PCET step,  $G_{R_n}$  was calculated following the Equation (1) [45]:

$$G_{R_n} = G_{\text{substrate} + C_{1-m}O_{2-2m-l}H_{n-2l}} + mCO_2 + lH_2O - G_{\text{substrate}} - G_{CO_2} - \frac{n}{2}G_{H_2} \quad (1)$$

where  $n$  represents the number of the transferred H<sup>+</sup>/e<sup>-</sup> (the  $n^{\text{th}}$  PCET step), and  $G_{\text{substrate} + C_{1-m}O_{2-2m-l}H_{n-2l}}$  represents the Gibbs free energy of the CO<sub>2</sub> reacted with  $n$  PCET steps. The Gibbs energy can be determined as  $G = H^0 - TS + \text{ZPE}$ , and the detail is displayed in ESI.

### 3. Results and Discussion

#### 3.1. The Basic Crystal and Electronic Structure of Double Halide Perovskite

CsPbBr<sub>3</sub> is one of the most typical cases of ABX<sub>3</sub> halide perovskites with face-centered cubic structure, and it shows promising properties in photocatalytic(electric) reaction. However, the Pb-based perovskite faces the bottlenecks of toxicity originating from the Pb ion. Up to date, Cs<sub>2</sub>AgInX<sub>6</sub> and Cs<sub>2</sub>AgBiX<sub>6</sub> (X = Cl, Br) have been demonstrated to be the next generation materials for substituting Pb-based halide perovskites [46], which are suitable for utilizing visible light. Consequently, we investigated the basic crystal and the electronic band structure of Cs<sub>2</sub>AgInCl<sub>6</sub>, Cs<sub>2</sub>AgInBr<sub>6</sub>, Cs<sub>2</sub>AgBiCl<sub>6</sub>, and Cs<sub>2</sub>AgBiBr<sub>6</sub> to find out whether these perovskites have potential in catalysis. In Figure 2a, the schematic of the substitution of Pb site and the corresponding primary cell of double halide perovskites are demonstrated. We construct the Pb-free double perovskite Cs<sub>2</sub>AgBiBr<sub>6</sub> via the replacement of the Pb site by Ag and Bi atoms on the basis of the origin CsPbBr<sub>3</sub> crystal structure. In spite of the heterovalent substitution on the Pb site, the monovalent of Ag and trivalent of Bi can maintain total charge neutrality. The radius of Ag and Bi atoms is 1.15 Å and 1.03 Å respectively, similar to the 1.19 Å of Pb atom, which can guarantee the stability of the substitutional structure. The high cubic symmetry in the primary cell of double perovskites is constructed by three different kinds of octahedrons [AgBr<sub>6</sub>]<sup>2-</sup>, [BiBr<sub>6</sub>]<sup>2-</sup> and [CsBr<sub>6</sub>]<sup>2-</sup>. The optimized crystal structure with the lowest energy is exhibited in Figure S1 in ESI. Similar to the basic structure perovskite of CsPbBr<sub>3</sub>, it is a three-dimension frame with *Fm-3m* space group symmetry, formed by corner connected octahedrons, and Cs<sup>+</sup> is at the octahedral interstices. For the double oxide perovskites, the rock-salt ordering is widely accepted as the ground state [47], and we believe it can also be adopted in the double halide perovskites [48]. After the lattice optimization, there is a small decrease of 3.69% in the cell parameter, compared with the original CsPbBr<sub>3</sub> (11.92 Å [49]). At the same time, the bond length of Ag-Br (3.20 Å) is larger than that of Bi-Br (2.88 Å) as the Br ions undergo a light displacement toward Bi ion, contributing to the relatively stronger attractive force of Bi<sup>3+</sup> than Ag<sup>+</sup>.

To better evaluate the feasibility as photocatalysts, the band structures of the reported double halide perovskites with the capacity in catalysis are investigated, including Cs<sub>2</sub>AgBiX<sub>6</sub> and Cs<sub>2</sub>AgInX<sub>6</sub> [50]. The band structures are displayed in Figure 2b. Obviously, there is an indirect bandgap in the Cs<sub>2</sub>AgBiX<sub>6</sub> system, while the Cs<sub>2</sub>AgInX<sub>6</sub> system possesses the direct bandgap like Pb-based CsPbCl<sub>3</sub> perovskite. For the Cs<sub>2</sub>AgBiX<sub>6</sub>, the bottom of the conduction band (CBM) and the top of the valence band (VBM) are located at L and X point, respectively. The CBM and VBM in Cs<sub>2</sub>AgInX<sub>6</sub> are both at  $\Gamma$  point. In the above computations, the spin-orbit coupling (SOC) is considered for all the double perovskites and shrinks the bandgap of Cs<sub>2</sub>AgBiX<sub>6</sub>. When SOC is involved in Cs<sub>2</sub>AgBiX<sub>6</sub> systems, the VBM and CBM can be more accurately determined as additional states will arise in the bandgap, leading to the downshift of the CBM [51]. As the halogen element changes from Cl to Br, the bandgap energy will undergo a decrease of 1.11 eV and 0.67 eV on Cs<sub>2</sub>AgBiX<sub>6</sub> and Cs<sub>2</sub>AgInX<sub>6</sub>, respectively. From the point of high-efficiency solar energy utilization, the Cs<sub>2</sub>AgBiCl<sub>6</sub> and Cs<sub>2</sub>AgInCl<sub>6</sub> exhibit relatively unsatisfactory ability as the utilized light wavelength is <514.52 nm and <478.76 nm, respectively. Remarkably, the band structure of

$\text{Cs}_2\text{AgInX}_6$  demonstrates the impropriety as the photocatalysts. Firstly, a relatively higher recombination rate of photo-induced carriers will be induced by the direct bandgap, resulting in the decrease in redox efficiency. Secondly, due to the parity-forbidden transition at band edges in highly centrosymmetric crystal structure, the optical adsorption may be severely reduced [52]. In the  $\text{Cs}_2\text{AgBiCl}_6$  system, the unique electronic structure can entirely overcome the above downsides. In addition, the comparison of typical Pb-free perovskites in respect to the lattice parameters and bandgaps is listed in Table 1. Although the organic perovskites exhibit a more satisfied bandgap for solar energy adsorption, they suffer from the weakness of instability. The type D perovskites (Figure 1) will face the challenge of decreased mobility of carriers [53,54]. Hence, the  $\text{Cs}_2\text{AgBiX}_6$  is adopted as the candidate for further adsorption investigation.

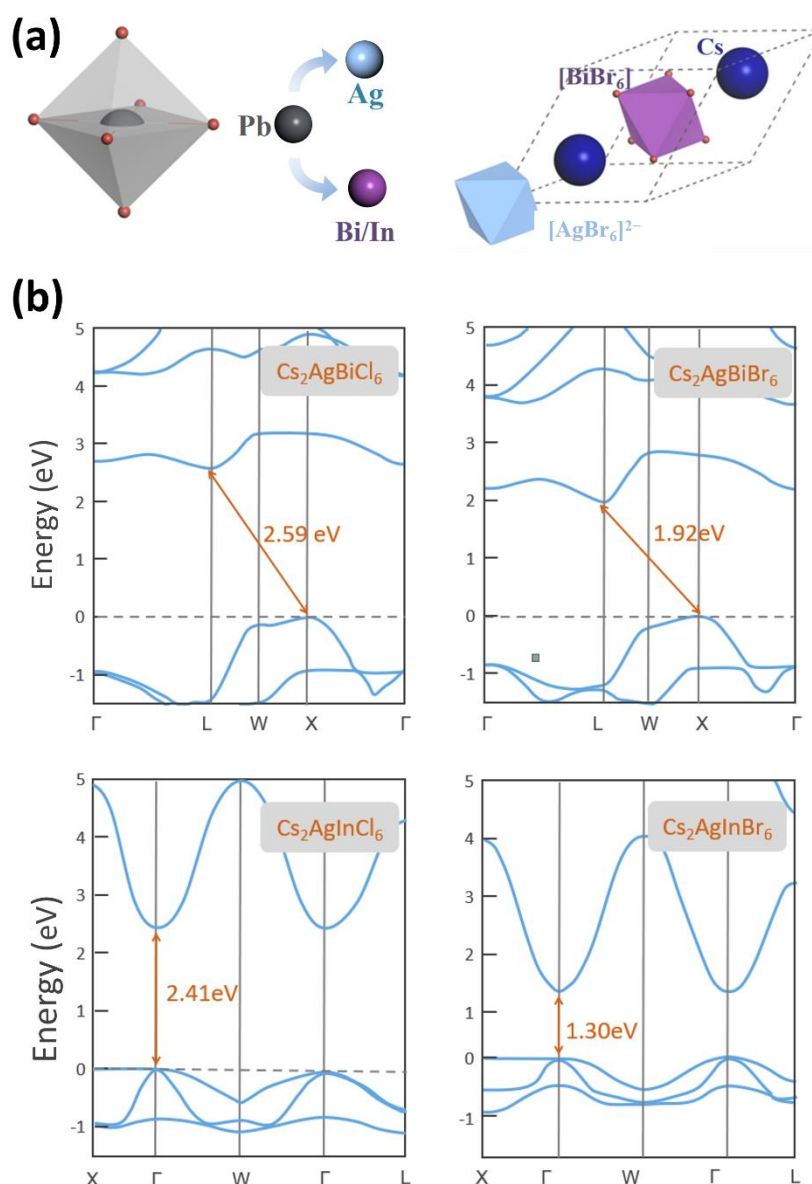


**Figure 2.** (a) Crystal construction strategy of  $\text{Cs}_2\text{AgBiBr}_6$  based on Pb-based halide perovskite  $\text{CsPbBr}_3$ . (b) The band structure of  $\text{Cs}_2\text{AgBiCl}_6$ ,  $\text{Cs}_2\text{AgBiBr}_6$ ,  $\text{Cs}_2\text{AgInCl}_6$  and  $\text{Cs}_2\text{AgInBr}_6$ .

**Table 1.** Structure information and bandgaps of typical Pb-free halide perovskites obtained from theoretical first-principle and experimental studies.

Perovskites	Space Group	Lattice Parameters (Å)	Band Gap (eV)		Ref.
			Theory	Experiment	
Cs <sub>2</sub> AgBiCl <sub>6</sub>	Fm3-m	10.51 (This work)	2.59 (This work)	2.41 (Ref. [55])	
Cs <sub>2</sub> AgBiBr <sub>6</sub>	Fm3-m	11.48 (This work)	1.92 (This work)	2.02 (Ref. [56])	
Cs <sub>2</sub> AgInCl <sub>6</sub>	Fm3-m	10.53 (This work)	2.41 (This work)	2.1 (Ref. [57])	
Cs <sub>2</sub> AgInBr <sub>6</sub>	Fm3-m	10.12 (This work)	1.30 (This work)	1.17 (Ref. [58])	
Cs <sub>2</sub> SnI <sub>6</sub>	Fm3-m	11.6276	1.3	1.26	[59]
		11.6276	1.6	1.62	[54]
		11.65	-	-	[60]
Cs <sub>2</sub> TiBr <sub>6</sub>	Fm3-m	10.92	0.89	-	[61]
Cs <sub>2</sub> TiBr <sub>6</sub> (@C <sub>60</sub> )			1.01	-	
Cs <sub>2</sub> TiI <sub>6</sub>	Fm3-m	11.67	0.79	-	[32]
CsRbSnI <sub>6</sub>	Pmn2 <sub>1</sub>	a = 8.2608	1.58	-	[62]
		b = 12.1507			
		c = 8.7913			
(CH <sub>3</sub> NH <sub>3</sub> ) <sub>2</sub> AgBiBr <sub>6</sub>	Fm3m	11.6370	2.02	2.02	[63]
(CH <sub>3</sub> NH <sub>3</sub> ) <sub>2</sub> KBiCl <sub>6</sub>	R3m	a = 7.8372	3.02	3.04	[64]
		c = 20.9938			

### 3.2. The Carbon Dioxide Capture Capacity on Modified Cs<sub>2</sub>AgBiBr<sub>6</sub>

It is worth noting that CO<sub>2</sub> conversion can be applied to gas processing for factory waste gas, automobile exhaust, useless gas from a laboratory. As such, we investigated the adsorption energy of CO, CO<sub>2</sub>, NO, and NO<sub>2</sub> to find out whether the CO<sub>2</sub> adsorption is energetically preferable. In order to build a stable foundation for the Cs<sub>2</sub>AgBiBr<sub>6</sub> framework, finding a suitable crystal termination plays an essential role for the following researches on surface catalytic reaction. Scientists have confirmed when employing room temperature in synthesis that the most stable surfaces of ABX<sub>3</sub> perovskite MAPbI<sub>3</sub> (tetragonal) are (001) and (110) [65,66]. While for the *Fm-3m* phase Cs<sub>2</sub>AgBiBr<sub>6</sub>, the (100) termination is equivalent to the (001) and (110) terminations of the tetragonal phase. From the view of charges, the (100) termination is nonpolar. Hence, Cs<sub>2</sub>AgBiBr<sub>6</sub> can be treated by composed layer by layer with TA (BiBr/AgBr<sub>3</sub>) and TB (CsX) (Figure 3a). The (2 × 1) supercell of the optimized double halide perovskite bulk was cleaved as a (100) surface to establish the slab model, as shown in Figure 3b. The slab and vacuum layer thickness are 18 Å and 15 Å respectively. This model can simulate the surface of the perovskite [67], because the supercell will repeat continuously in the *x-y* plane while the vacuum layer can break the continuity in the *z*-direction. In fact, a systematic research on the termination has been given, and the TB is always favored irrespective of the CsBr availability [67]. To design a prominent photocatalytic material employed at ambient conditions, the rational selection of the terminal surfaces determines the electronic local environment on active sites. As such, we adopt TB to investigate the adsorption performance on the CO, CO<sub>2</sub>, NO, and NO<sub>2</sub>, which are the major compositions in the industry exhaust and adverse to the atmosphere. At the same time, surface modification has been revealed to promote the adsorption and catalytic performance [68–71], so we investigate the effect of Cl, I and Br-vacancy doping on Cs<sub>2</sub>AgBiBr<sub>6</sub> surface. Displayed in Figure 3c, there are two different sites (site 1 and site 2) of Br in TB, thus defect formation energy are calculated to ascertain the energetically preferable doping sites following the Equation (2) [72]:

$$E^f(D) = E_{tot}(D) - E_{host}(U) - \sum_i n_i \mu_i \quad (2)$$

where  $E_{tot}(D)$  and  $E_{host}(U)$  represents the energy of the doped system and undoped system,  $n_i$  are the amounts of atoms added or removed from the host material to create the defect,  $\mu_i$  are the chemical potentials of these atoms. Results demonstrate that Br-vacancy

exhibits the smallest  $E^f(D)$  of 3.47 eV in Site 2, which is close to the previous work in halide and oxide perovskites [73–75]. The Cl, I, and Br-vacancy are calculated to be relatively more stable to locate at Site 1, Site 1, and Site 2 respectively (detailed  $E^f(D)$  information is concluded in Table S1 in ESI). The doped structures after structure optimization are displayed in Figure 3c.

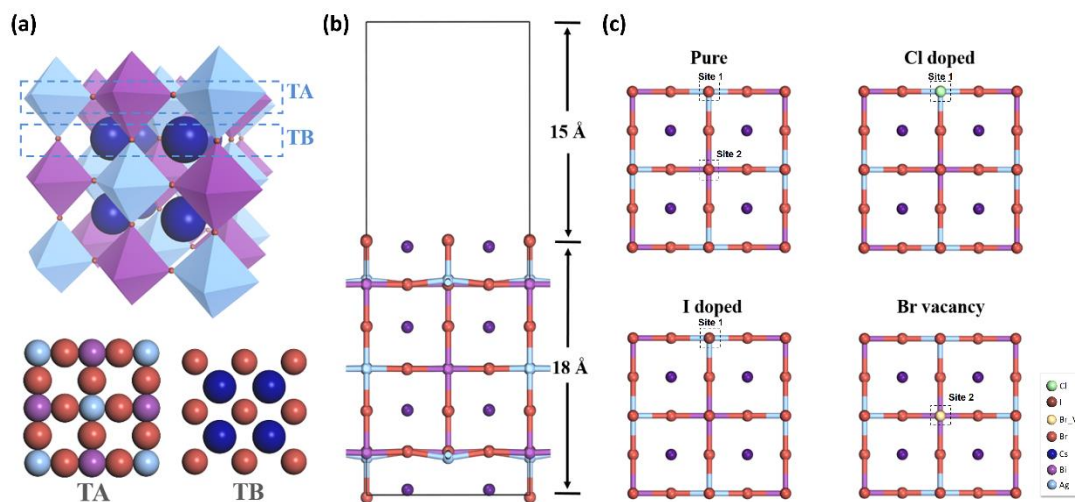


**Figure 3.** (a) Different terminates (TA, TB) of Cs<sub>2</sub>AgBiBr<sub>6</sub>. (b) The side view of the pure Cs<sub>2</sub>AgBiBr<sub>6</sub> surface slab. (c) The corresponding top view of the pure surface slab (which contains two different sites of Br) as well as the Cl doped, I doped and Br-vacancy system after structure optimization.

The outcomes are of great importance as steady adsorption is the prerequisite of the next step in photocatalysis because the core of gas capture is changing the electronic properties of the whole system. As is demonstrated in Figure 4, the adsorption performance of CO, CO<sub>2</sub>, NO, NO<sub>2</sub>, in pure Cs<sub>2</sub>AgBiBr<sub>6</sub> and the corresponding Cl doped, I doped, and Br-vacancy system are comprehensively investigated. To obtain the optimal structure, we consider unique adsorption sites and the orientation of gas molecular. Figure 4 displays all the optimized structure in those systems and the corresponding structural details are concluded in Table 2. We found that the O atom is attended to approach to Cs atom (as the relative high ability of O in obtaining charges and Cs in losing charges), which gives the foundation of gas molecular spontaneously adsorbed on the surface. The distance between two-O-atom molecules (NO<sub>2</sub> and CO<sub>2</sub>) and the Cs<sub>2</sub>AgBiBr<sub>6</sub> surface are shorter than that of one-O-atom molecules (CO and NO), and the bond length in every gas molecule is increased. Figure 5 shows the adsorption energy and bond length of each gas molecular after the structural optimization. The pure surface and the modified surface are adopted as the substrate. Nearly all of the system exhibit spontaneous adsorption of the gas molecules demonstrated from the negative value of  $E_b$ . It is widely accepted when  $|E_b| < 0.5$  eV the adsorption process can be treated as physical adsorption, when  $|E_b| > 0.5$  eV it can be treated as chemical adsorption [76]. In this regard, the Br-vacancy perovskite can lead to the chemical adsorption of all gas molecules with the minimum value of  $|E_b|$  calculated to be 0.77 eV. In Figure 5a, the pure Cs<sub>2</sub>AgBiBr<sub>6</sub> shows the slight adsorption of NO, NO<sub>2</sub>, CO and CO<sub>2</sub> with the range of  $E_b$  from  $-0.38$  eV to  $-0.01$  eV. The halide dopant systems (Cl doped and I doped) both exhibit insignificant improvement in adsorption. On the other hand, the adsorption energy of NO, NO<sub>2</sub>, CO and CO<sub>2</sub> on Br-vacancy Cs<sub>2</sub>AgBiBr<sub>6</sub> are within  $-1.2$  eV to  $-0.7$  eV, much more negative than the pure and halide dopant systems. According to the previous research [77], the vacancy can accumulate massive charge on the center of the site, playing a critical role in activating adsorption species. On the other hand, the CO<sub>2</sub> adsorption energy in all the Cs<sub>2</sub>AgBiBr<sub>6</sub> systems is the lowest compared with other gas, implying the Cs<sub>2</sub>AgBiBr<sub>6</sub> materials prefer to capture CO<sub>2</sub> from the exhaust gas containing carbides and nitrides. Figure 5b demonstrates the bond length of each gas

molecular on the different systems. Notably, the bonding in CO<sub>2</sub> captured with the system with Br vacancy elongate most compared with the pure and dopant systems, which can illustrate the strong chemical adsorption between the CO<sub>2</sub> and the vacancy site with the  $E_b$  of  $-1.12$  eV.

**Table 2.** Conclusion of structure information before and after gas molecular adsorbed on the substrate.

Pervskite	Gas	$E_b$ (eV)	Bond Length of Gas Molecular (Å)		Bond Angle of Gas Molecular (°)	
			Original	Adsorbed	Original	Adsorbed
Pure	NO	-0.33	1.15	1.17	/	/
	NO <sub>2</sub>	-0.01	1.20	1.27, 1.22	134.3	127.47
	CO	-0.13	1.13	1.13	/	/
	CO <sub>2</sub>	-0.38	1.16	1.17, 1.17	180.0	176.75
Cl doped	NO	-0.28	1.15	1.16	/	/
	NO <sub>2</sub>	-0.12	1.20	1.27, 1.22	134.3	127.47
	CO	-0.27	1.13	1.14	/	/
	CO <sub>2</sub>	-0.46	1.16	1.17, 1.17	180.0	179.55
I doped	NO	0.027	1.15	1.17	/	/
	NO <sub>2</sub>	-0.18	1.20	1.23, 1.23	134.3	126.63
	CO	0.12	1.13	1.14	/	/
	CO <sub>2</sub>	-0.26	1.16	1.17, 1.17	180.0	/
Br vacancy	NO	-1.00	1.15	1.24	/	/
	NO <sub>2</sub>	-1.11	1.20	1.19, 1.15	134.3	149.71
	CO	-0.77	1.13	1.14	/	/
	CO <sub>2</sub>	-1.12	1.16	1.28, 1.24	180.0	143.15

Moreover, the charge transfer is considered, aiming to probe into the degree of association between surface and gas molecular in respect of charges. The charge loss of pure Cs<sub>2</sub>AgBiBr<sub>6</sub> is  $-0.055$  eV,  $-0.414$  eV,  $-0.023$  eV, and  $-0.316$  eV after the adsorption of NO, NO<sub>2</sub>, CO, and CO<sub>2</sub>, which exhibit the strong ability of NO<sub>2</sub> and CO<sub>2</sub> on attracting electrons.

### 3.3. The Pure Cs<sub>2</sub>AgBiBr<sub>6</sub> for CO<sub>2</sub> Catalytic Performance

Considering the end-on CO<sub>2</sub> adsorption and the unique surface on Cs<sub>2</sub>AgBiBr<sub>6</sub>, the CO<sub>2</sub> reduction process follows the complicated reaction pathways, as is presented in Figure 6a. For each step, the H<sup>+</sup>/e<sup>-</sup> pairs participates in the species' protonation either on C or O atoms. Since two adjacent Cs atoms are separated by halide atoms, the double carbon products are unable to generate. The single carbon products (i.e., CH<sub>4</sub>, HCOOH, CH<sub>3</sub>OH, CO) can be obtained via the regulation of combination sites in PCET steps and the exact amount of H<sup>+</sup>/e<sup>-</sup> pairs participated in the reaction. If one CO<sub>2</sub> molecular is only reduced by singular numbers of H<sup>+</sup>/e<sup>-</sup> pairs, the whole system will be in an energetically unstable transition state, resulting in the next PCET step spontaneously. In this paper, we focus on the single carbon products. The CO and HCOOH molecules need two electrons in reaction, while CH<sub>3</sub>OH belongs to the six-electron reaction and the CH<sub>4</sub> is the eight-electron product. Massive intermediates are involved in the CO<sub>2</sub> reduction process. We optimized all the possible species in the pure Cs<sub>2</sub>AgBiBr<sub>6</sub>, and the most energetically favored reaction paths were obtained. The configurations of the intermediates with the lowest energy are displayed in Figure 6b, which compose the optimal reaction pathway. And the free energy profile of the whole system is displayed in Figure 6c. The reaction path is based on the largest amount of H<sup>+</sup>/e<sup>-</sup> pairs (eight) participating in the catalysis process and enough energy applied to support overcoming the energy barrier in each PCET step, especially when an odd number of H<sup>+</sup>/e<sup>-</sup> pairs is induced. It was found that the products of HCOOH, H<sub>2</sub>C(OH)<sub>2</sub>, H<sub>2</sub>COH, and CH<sub>4</sub> were obtained. In the pure Cs<sub>2</sub>AgBiBr<sub>6</sub> system, CO<sub>2</sub> is firstly held by one Cs atom exposed on the TB surface, and the CO<sub>2</sub> end-on model, which is fixed by two Cs atoms, has been proven to be energy-unfavorable. The first PCET step



is to form highly symmetrical  $\text{HCO}_2^-$  with the free energy change of +1.23 eV. The next triple  $\text{H}^+$  additions mainly concentrate on one O atom beside the Cs atom, and the  $\text{H}_2\text{O}$  is firstly released. The corresponding values of  $\Delta G$  are  $-1.45$  eV,  $+1.43$  eV and  $-1.88$  eV. Then, the remaining  $\text{H}_2\text{CO}$  undergoes triple protonation, and the  $\text{CH}_4$  is released with the free energy change of  $+2.07$  eV,  $-1.65$  eV and  $+2.68$  eV. Finally, OH forms  $\text{H}_2\text{O}$  with the declined free energy change of  $-2.32$  eV. In the pure  $\text{Cs}_2\text{AgBiBr}_6$  system, the change of free energy ranges largely, implying the  $\text{CO}_2$  reduction process is massively exergonic, and the main product is  $\text{CH}_4$ . The potential determining step (PDS) is  $\text{H}_3\text{COH} + \text{H}^+ \rightarrow \text{OH}^- + \text{CH}_4\uparrow$ . This step is regarded as the crucial step for  $\text{CH}_4$  desorption, requiring overcoming barrier energy of 2.68 eV.

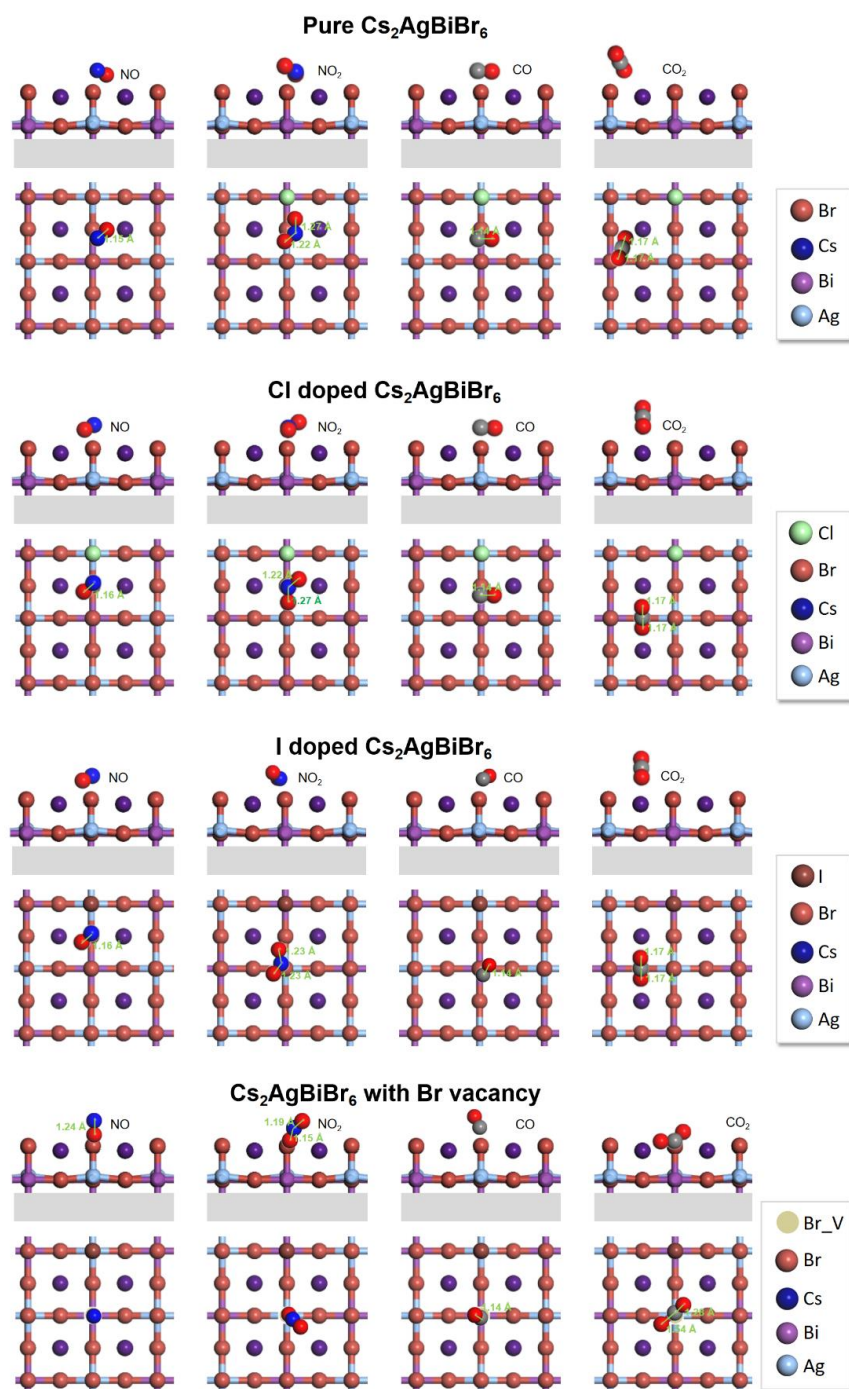


**Figure 4.** The adsorption configuration of four unique gas molecular on the pure, Cl doped, I doped, and vacancy doped  $\text{Cs}_2\text{AgBiBr}_6$ .

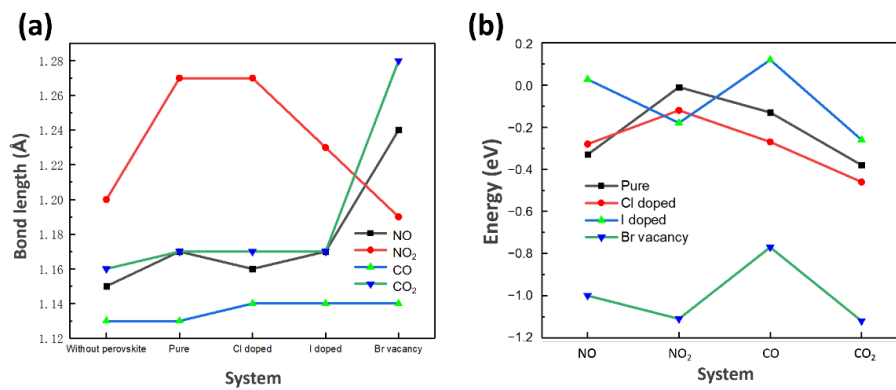


**Figure 5.** (a) The adsorption energy and (b) the bond length of four gas molecular on the pure, Cl doped, I doped and vacancy doped Cs<sub>2</sub>AgBiBr<sub>6</sub>.

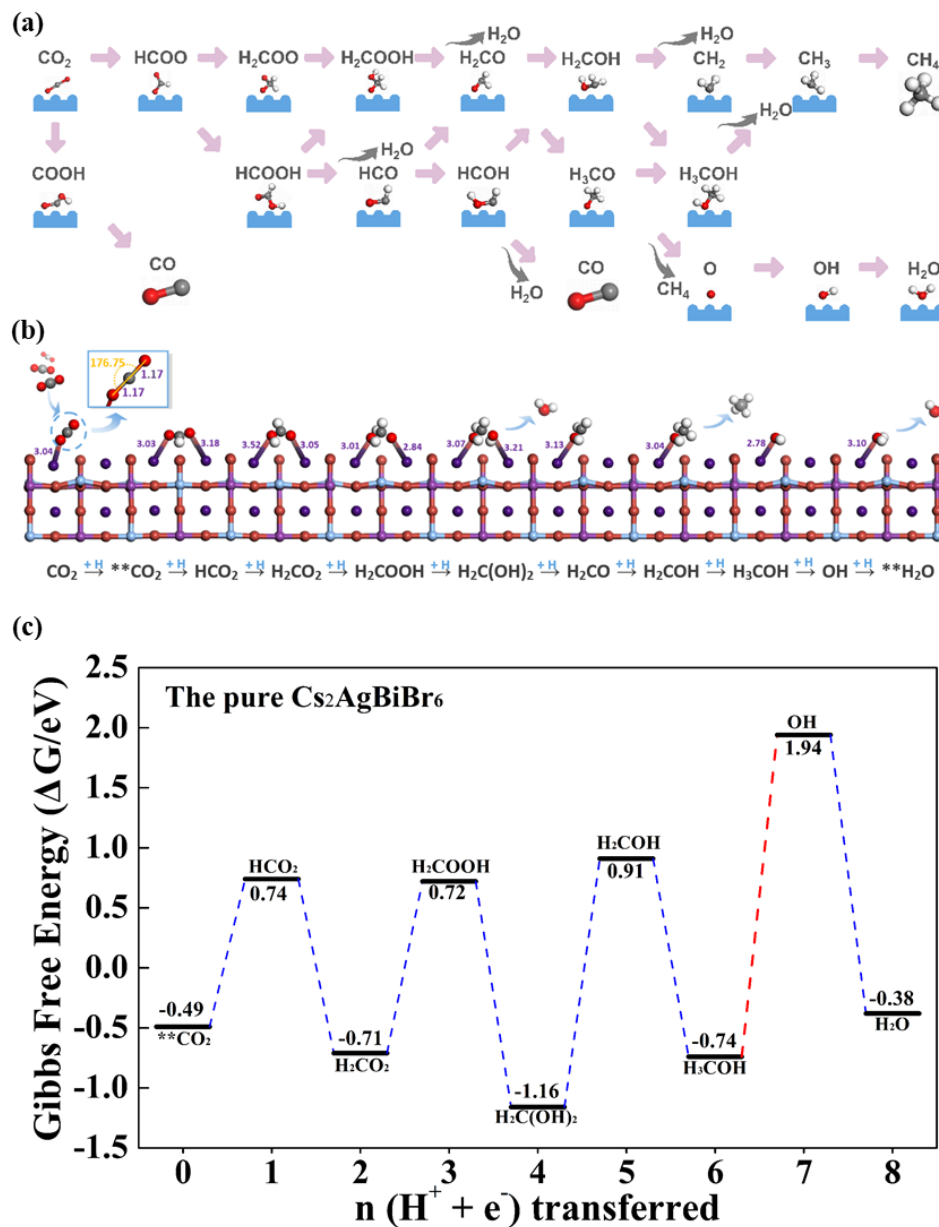


**Figure 6.** (a) Possible reaction path for CO<sub>2</sub> reduction. (b) All the optimized intermediates on the pure Cs<sub>2</sub>AgBiBr<sub>6</sub>. (c) The calculated minimum free energy profile for the pure Cs<sub>2</sub>AgBiBr<sub>6</sub>.

### 3.4. The Vacancy and Doping Engineering for the Improved CO<sub>2</sub> Catalytic Performance

Due to the relatively large barrier of CO<sub>2</sub>RR, it is imperative to modulate the intrinsic electronic properties of Cs<sub>2</sub>AgBiBr<sub>6</sub> to enhance the catalytic activity. Vacancy and halogen doping are regarded as two electronic structure designing strategies and make a contributor to the adsorption of the intermediates. Hence, the detailed CO<sub>2</sub>RR process on Cs<sub>2</sub>AgBiBr<sub>6</sub> with Cl dopant, I dopant and Br-vacancy on the TB is systematically explored (Figure 7).

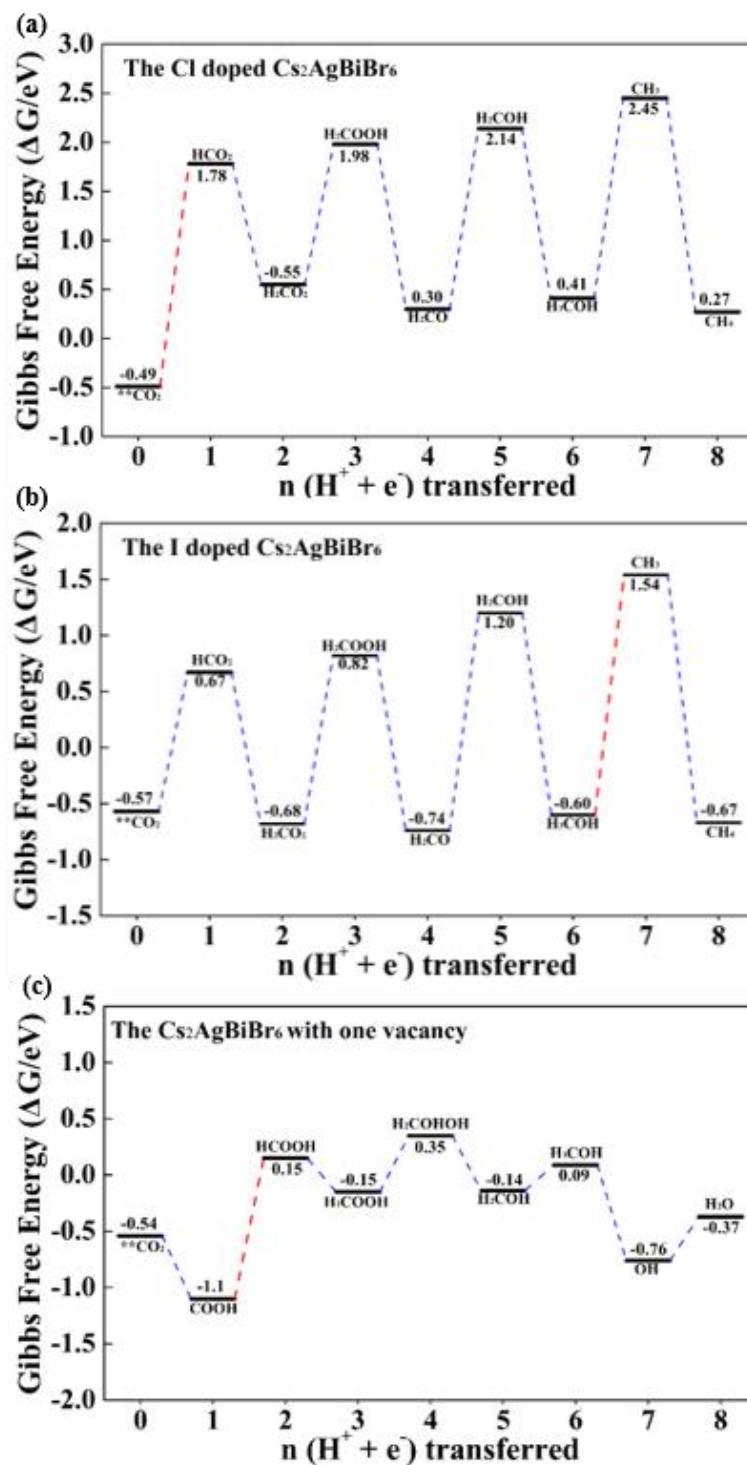
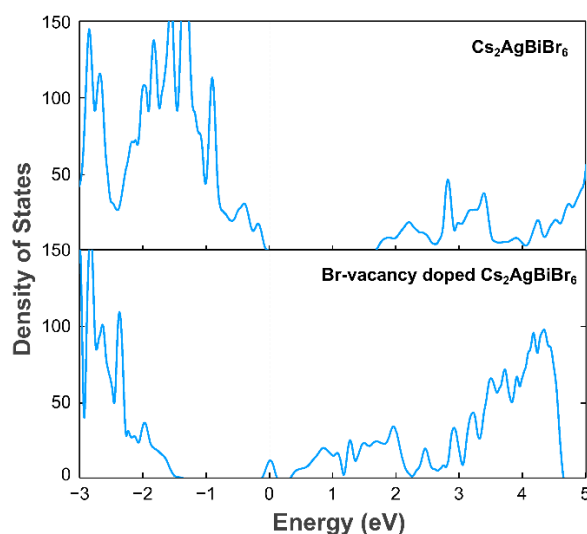


Figure 7. The calculated minimum free energy profile for the Cs<sub>2</sub>AgBiBr<sub>6</sub> with (a) Cl dopant, (b) I dopant and (c) one vacancy on the TB.

In the halide-doped systems (Figure 7a,b), the optimized CO<sub>2</sub> reduction pathway follows  $^{**}\text{CO}_2 \rightarrow \text{HCO}_2 \rightarrow \text{H}_2\text{CO}_2 \rightarrow \text{H}_2\text{COOH} \rightarrow \text{H}_2\text{CO} \rightarrow \text{H}_2\text{COH} \rightarrow \text{H}_3\text{COH} \rightarrow \text{CH}_3 \rightarrow \text{CH}_4$ , demonstrating the similarity to the pure Cs<sub>2</sub>AgBiBr<sub>6</sub>. However, when the H<sub>3</sub>COH species is protonated, the H<sup>+</sup>/e<sup>-</sup> pairs are inclined to add on O atom. In the Cl and I dopant systems, the H<sub>2</sub>O is firstly released with the increasing free energy of 2.04 eV and 2.14 eV. The value of the seventh PCET step is smaller than that of +2.68 eV in the pure system, which can better illustrate that the halide dopant plays a significant role in the decrease of the active barrier. The final product, CH<sub>4</sub>, is generated from the attack of H<sup>+</sup>/e<sup>-</sup> pairs to the CH<sub>3</sub> species. Owing to the high activation in CH<sub>3</sub> species, this step results in the high stability of the reactant CH<sub>4</sub> with the distinct downhill free energy change of -2.13 eV and -2.21 eV. CH<sub>4</sub> is still captured by the Cs site, and the adsorption energy of CH<sub>4</sub> on Cl and I dopant systems are -0.14 eV and -1.02 eV, respectively. For the I dopant system, the adsorption energy is too low, which will indicate the suppressed process of desorption. In comparison, the moderate adsorption energy of CH<sub>4</sub> on the Cl dopant system demonstrates the advantages in adsorption and desorption for CO<sub>2</sub>RR. The PDSs in Cl and I dopant systems are respectively  $^{**}\text{CO}_2 \rightarrow \text{HCO}_2$  and  $\text{H}_3\text{COH} \rightarrow \text{CH}_3$ , requiring the energy input of 2.27 eV and 2.14 eV. In spite of the fact that halide doping further activates the species in CO<sub>2</sub>RR process, the improved efficiency is insignificant, and the value of PDS is still above 2 eV.

Considering the vacancies often formed in experiments, continued computation via the optimized free energy profile for catalytic CO<sub>2</sub> reduction on the Cs<sub>2</sub>AgBiBr<sub>6</sub> with one vacancy was carried out and the reaction path is shown in Figure 7c. Distinguished from the pure and halide dopant system, the pathway on Br-vacancy Cs<sub>2</sub>AgBiBr<sub>6</sub> follows  $^{**}\text{CO}_2 \rightarrow \text{COOH} \rightarrow \text{HCOOH} \rightarrow \text{H}_2\text{COOH} \rightarrow \text{H}_2\text{COHOH} \rightarrow \text{H}_2\text{COH} \rightarrow \text{H}_3\text{COH} \rightarrow \text{OH} + \text{CH}_4 \rightarrow \text{H}_2\text{O}$ . The first two PCET steps produce the new intermediates HCOOH with the maximal barrier of 1.25 eV. In the next two steps, H<sup>+</sup>/e<sup>-</sup> pairs are prior to occupy the C atom and then add to the O atom. After the formation of H<sub>2</sub>O, there are still two H atoms connected with C atom, thus the next two PCET steps prompt the release of CH<sub>4</sub>. Obviously, the free energy range of the whole intermediates in CO<sub>2</sub> reduction maintains in a small scale. The PDS is the process of COOH to form HCOOH (1.25 eV), and this value is comparable to the Au catalyst [78] and sulfur-doped g-C<sub>3</sub>N<sub>4</sub> [79] for CO<sub>2</sub> reduction. This relative low barrier of PDS predicts the smooth CO<sub>2</sub> conversion in Cs<sub>2</sub>AgBiBr<sub>6</sub> with vacancies.

To reveal the effect of Br-vacancy on the electronic property of Cs<sub>2</sub>AgBiBr<sub>6</sub>, we calculated the density of states (DOS) for pure and Br-vacancy Cs<sub>2</sub>AgBiBr<sub>6</sub> surface using the method of GGA-PBE. From Figure 8, it can be deduced that the forming of Br-vacancy can move the Fermi level from VBM to near the CBM, which is consistent with previous work on studying the O-vacancy and Cl-vacancy [80–82]. As the peak introduced by defective states is sharp and separated from the relatively delocalized electrons in the conduction band, the exceeding electrons brought by vacancy are localized. It widely acknowledged that deep-level impurity can act as the recombination center for carriers, which will lead to the deactivation of catalysts. The vacancy adopted in this work introduces the extra defective electronic states located very close to the CBM, which can be defined as shallow doping energy level, thus not expected to accelerate the catalysis deactivation. In addition, although the vacancy decreases the bandgap energy, such a slight decrease in bandgap will have minor effects on the conversion of carriers [83].



**Figure 8.** DOS plot for  $\text{Cs}_2\text{AgBiBr}_6$  and Br-vacancy doped  $\text{Cs}_2\text{AgBiBr}_6$ .

#### 4. Conclusions

In summary, employing the well-resolved DFT calculations, we concentrate on the comprehensive investigation in the  $\text{Cs}_2\text{AgBiBr}_6$  as the novel  $\text{CO}_2$  reduction catalyst. Based on the structure of  $\text{CsPbBr}_3$ ,  $\text{Ag}^+/\text{Bi}^{3+}$  and  $\text{Ag}^+/\text{In}^{3+}$  are adopted to substitute  $\text{Pb}^{2+}$  to realize the objection on Pb-free, keeping the crystal stable and the charge balance. The  $\text{Cs}_2\text{AgBiBr}_6$ , of which the bandgap is calculated to be 1.92 eV, is determined to be the most potential material for  $\text{CO}_2$ RR. Further studies on CO,  $\text{CO}_2$ , NO,  $\text{NO}_2$ , gas capture proved  $\text{Cs}_2\text{AgBiBr}_6$  a suitable material for  $\text{CO}_2$  adsorption and the doping and vacancy-doped systems still demonstrate the simultaneous tendency for  $\text{CO}_2$  preference. Moreover, the detailed  $\text{CO}_2$ RR pathway on the pure, Cl-doped, I-doped and Br-vacancy  $\text{Cs}_2\text{AgBiBr}_6$  are studied with the judgment of Gibbs free energy. The vacancy-doping system could significantly promote the procedure with the potential determining step (PDS) of 1.25 eV, compared with 2.68 eV of pure system, 2.27 eV of Cl-doped system and 2.14 eV of I-doped system. Further investigation of the  $\text{Cs}_2\text{AgBiBr}_6$  with Br-vacancy reveals that the vacancy will not obviously promote the process of catalysis deactivation, as there is no formation of deep-level electronic states acting as carrier recombination center. In this regard, this work paves a potential avenue in demystifying the defect modification mechanism on lead-free halide double perovskites, which will lay a foundation for defect engineering in  $\text{CO}_2$ RR photocatalysts toward a host of environmental and energetic applications.

**Supplementary Materials:** The following are available online at <https://www.mdpi.com/article/10.3390/ma14102469/s1>, The illustration of NHE (Normal Hydrogen Electrode), The calculation of Gibbs free energy, Figure S1: Scheme of the optimized crystal structure and two types of Br, which can be doped by Cl and I, Table S1:  $E^f(D)$  values calculated for Cl, I, Br-vacancy doped in Site 1 and Site 2.

**Author Contributions:** Formal analysis, P.C., Y.H. and Z.S.; Investigation, P.C. and Y.H.; Resources, Y.H.; Software, Y.H.; Supervision, N.L.; Writing—original draft, X.C., P.C.; Writing—review & editing, P.C., Y.H. and N.L. All authors have read and agreed to the published version of the manuscript.

**Funding:** This research was funded by the Fok Ying-Tong Education Foundation for Young Teachers in the Higher Education Institutions of China (No. 161008); the Natural Science Fund for Distinguished Young Scholars of Hubei Province grant number 2020CFA087; the Basic Research Program of Shenzhen grant number JCYJ20190809120015163; the Overseas Expertise Introduction Project (111 project) for Discipline Innovation of China grant number B18038; the State Key Laboratory of Refractories and Metallurgy of Wuhan University of Science and Technology grant number G201605; the Research Fund from the Center of Innovation and Entrepreneurship of Wuhan University of Technology grant number S2020001026.

**Institutional Review Board Statement:** Not applicable.

**Informed Consent Statement:** Not applicable.

**Data Availability Statement:** The data presented in this study are available on request from the corresponding author.

**Acknowledgments:** N.L. thanks for the supported by the Fok Ying-Tong Education Foundation for Young Teachers in the Higher Education Institutions of China (No. 161008); the Natural Science Fund for Distinguished Young Scholars of Hubei Province (No. 2020CFA087); the Basic Research Program of Shenzhen (No. JCYJ20190809120015163); the Overseas Expertise Introduction Project (111 project) for Discipline Innovation of China (B18038); the State Key Laboratory of Refractories and Metallurgy of Wuhan University of Science and Technology (No. G201605); The authors acknowledge Beijing PARATERA Tech CO., Ltd. for providing HPC resources that have contributed to the research results reported within this work. P.C. would like to acknowledge assistance, faculty start-up supports, and Research Fund (No. S2020001026) from the Center of Innovation and Entrepreneurship of Wuhan University of Technology ([https://www.x-mol.com/groups/WUT\\_CIE.com](https://www.x-mol.com/groups/WUT_CIE.com)).

**Conflicts of Interest:** The authors declare no conflict of interest.

## References

1. Wang, W.; Tade, M.O.; Shao, Z.P. Research Progress of Perovskite Materials in Photocatalysis- and Photovoltaics-Related Energy Conversion and Environmental Treatment. *Chem. Soc. Rev.* **2015**, *44*, 5371–5408. [[CrossRef](#)]
2. Vautier, M.; Guillard, C.; Herrmann, J.-M. Photocatalytic Degradation of Dyes in Water: Case Study of Indigo and of Indigo Carmine. *J. Catal.* **2001**, *201*, 46–59. [[CrossRef](#)]
3. He, H.; Zhong, M.; Yacatto, K.; Rappold, T.; Sugar, G.; David, N.E.; Gelb, J.; Kotwal, N.; Merkle, A.; Konkolewicz, D.; et al. Three-Dimensionally Ordered Macroporous Polymeric Materials by Colloidal Crystal Templating for Reversible CO<sub>2</sub> Capture. *Adv. Funct. Mater.* **2013**, *23*, 4720–4728. [[CrossRef](#)]
4. Zhang, C.; Cao, M.; Ma, H.; Yu, C.; Li, K.; Yu, C.; Jiang, L. Morphology-Control Strategy of the Superhydrophobic Poly(Methyl Methacrylate) Surface for Efficient Bubble Adhesion and Wastewater Remediation. *Adv. Funct. Mater.* **2017**, *27*, 1702020. [[CrossRef](#)]
5. Phuan, Y.W.; Ong, W.-J.; Chong, M.N.; Ocon, J.D. Prospects of Electrochemically Synthesized Hematite Photoanodes for Photoelectrochemical Water Splitting: A Review. *J. Photochem. Photobiol. C Photochem. Rev.* **2017**, *33*, 54–82. [[CrossRef](#)]
6. Zhang, C.; Zhao, P.; Liu, S.; Yu, K. Three-Dimensionally Ordered Macroporous Perovskite Materials for Environmental Applications. *Chin. J. Catal.* **2019**, *40*, 1324–1338. [[CrossRef](#)]
7. Abe, R.; Shinmei, K.; Hara, K.; Ohtani, B. Robust Dye-Sensitized Overall Water Splitting System With Two-Step Photoexcitation of Coumarin Dyes and Metal Oxide Semiconductors. *Chem. Commun.* **2009**, *24*, 3577. [[CrossRef](#)]
8. Abe, R.; Takata, T.; Sugihara, H.; Domen, K. Photocatalytic Overall Water Splitting under Visible Light by TaON and WO<sub>3</sub> With an IO<sub>3</sub><sup>-</sup>/I<sup>-</sup> Shuttle Redox Mediator. *Chem. Commun.* **2005**, *30*, 3829–3831. [[CrossRef](#)] [[PubMed](#)]
9. Adhikari, S.P.; Hood, Z.D.; More, K.L.; Chen, V.W.; Lachgar, A. A Visible-Light-Active Heterojunction with Enhanced Photocatalytic Hydrogen Generation. *ChemSusChem* **2016**, *9*, 1869–1879. [[CrossRef](#)]
10. Andrei, V.; Hoye, R.L.Z.; Crespo-Quesada, M.; Bajada, M.; Ahmad, S.; De Volder, M.; Friend, R.; Reisner, E. Scalable Triple Cation Mixed Halide Perovskite-BiVO<sub>4</sub> Tandems for Bias-Free Water Splitting. *Adv. Energy Mater.* **2018**, *8*, 1801403. [[CrossRef](#)]
11. Ni, G.; Chen, S.; Sunku, S.S.; Sternbach, A.; McLeod, A.S.; Xiong, L.; Fogler, M.M.; Chen, G.; Basov, D.N. Nanoscale Infrared Spectroscopy and Imaging of Catalytic Reactions in Cu<sub>2</sub>O Crystals. *ACS Photon.* **2020**, *7*, 576–580. [[CrossRef](#)]
12. Zhang, Z.; Wu, H.; Yu, Z.; Song, R.; Qian, K.; Chen, X.; Tian, J.; Zhang, W.; Huang, W. Site-Resolved Cu<sub>2</sub>O Catalysis in the Oxidation of CO. *Angew. Chem. Int. Ed.* **2019**, *58*, 4276–4280. [[CrossRef](#)] [[PubMed](#)]
13. Jiang, N.; Li, X.; Guo, H.; Li, J.; Shang, K.; Lu, N.; Wu, Y. Plasma-Assisted Catalysis Decomposition of BPA over Graphene-CdS Nanocomposites in Pulsed Gas-Liquid Hybrid Discharge: Photocorrosion Inhibition and Synergistic Mechanism Analysis. *Chem. Eng. J.* **2021**, *412*, 128627. [[CrossRef](#)]
14. Zhang, M.; Hu, Q.; Ma, K.; Ding, Y.; Li, C. Pyroelectric Effect in CdS Nanorods Decorated With a Molecular Co-Catalyst for Hydrogen Evolution. *Nano Energy* **2020**, *73*, 104810. [[CrossRef](#)]
15. Nasir, M.S.; Yang, G.; Ayub, I.; Wang, S.; Yan, W. Tin Diselenide a Stable Co-Catalyst Coupled With Branched TiO<sub>2</sub> Fiber and G-C<sub>3</sub>N<sub>4</sub> Quantum Dots for Photocatalytic Hydrogen Evolution. *Appl. Catal. B Environ.* **2020**, *270*, 118900. [[CrossRef](#)]
16. Zhuang, Z.; Li, Y.; Li, Z.; Lv, F.; Lang, Z.; Zhao, K.; Zhou, L.; Moskaleva, L.; Guo, S.; Mai, L. MoB/G-C<sub>3</sub>N<sub>4</sub> Interface Materials as a Schottky Catalyst to Boost Hydrogen Evolution. *Angew. Chem. Int. Ed.* **2018**, *57*, 496–500. [[CrossRef](#)] [[PubMed](#)]
17. Marszewski, M.; Cao, S.; Yu, J.; Jaroniec, M. Semiconductor-Based Photocatalytic CO<sub>2</sub> Conversion. *Mater. Horiz.* **2015**, *2*, 261–278. [[CrossRef](#)]
18. Shen, J.; Kolb, M.J.; Göttle, A.J.; Koper, M.T.M. DFT Study on the Mechanism of the Electrochemical Reduction of CO<sub>2</sub> Catalyzed by Cobalt Porphyrins. *J. Phys. Chem. C* **2016**, *120*, 15714–15721. [[CrossRef](#)]

19. Qin, B.; Zhang, Q.; Li, Y.; Yang, G.; Yu, H.; Peng, F. Mechanistic Insights into the Electrochemical Reduction of CO<sub>2</sub> on Cyclocarbon Using Density Functional Theory Calculations. *ChemElectroChem* **2020**, *7*, 1838–1842. [[CrossRef](#)]
20. Vijay, S.; Gauthier, J.A.; Heenen, H.H.; Bukas, V.J.; Kristoffersen, H.H.; Chan, K. Dipole-Field Interactions Determine the CO<sub>2</sub> Reduction Activity of 2D Fe–N–C Single-Atom Catalysts. *ACS Catal.* **2020**, *10*, 7826–7835. [[CrossRef](#)]
21. Hong, Z.; Chong, W.K.; Ng, A.Y.R.; Li, M.; Ganguly, R.; Sum, T.C.; Soo, H.S. Hydrophobic Metal Halide Perovskites for Visible-Light Photoredox C–C Bond Cleavage and Dehydrogenation Catalysis. *Angew. Chem. Int. Ed.* **2019**, *58*, 3456–3460. [[CrossRef](#)]
22. Huang, H.; Yuan, H.; Zhao, J.; Solís-Fernández, G.; Zhou, C.; Seo, J.W.; Hendrix, J.; Debroye, E.; Steele, J.A.; Hofkens, J.; et al. C(sp<sup>3</sup>)–H Bond Activation by Perovskite Solar Photocatalyst Cell. *ACS Energy Lett.* **2019**, *4*, 203–208. [[CrossRef](#)]
23. Huang, X.; Zhao, G.; Wang, G.; Irvine, J.T.S. Synthesis and Applications of Nanoporous Perovskite Metal Oxides. *Chem. Sci.* **2018**, *9*, 3623–3637. [[CrossRef](#)] [[PubMed](#)]
24. Kong, J.; Yang, T.; Rui, Z.; Ji, H. Perovskite-Based Photocatalysts for Organic Contaminants Removal: Current Status and Future Perspectives. *Catal. Today* **2019**, *327*, 47–63. [[CrossRef](#)]
25. Kovalenko, M.V.; Protesescu, L.; Bodnarchuk, M.I. Properties and Potential Optoelectronic Applications of Lead Halide Perovskite Nanocrystals. *Science* **2017**, *358*, 745–750. [[CrossRef](#)] [[PubMed](#)]
26. Babayigit, A.; Ethirajan, A.; Muller, M.; Conings, B. Toxicity of Organometal Halide Perovskite Solar Cells. *Nat. Mater.* **2016**, *15*, 247–251. [[CrossRef](#)]
27. Babayigit, A.; Thanh, D.D.; Ethirajan, A.; Manca, J.; Muller, M.; Boyen, H.G.; Conings, B. Assessing the Toxicity of Pb- and Sn-Based Perovskite Solar Cells in Model Organism *Danio rerio*. *Sci. Rep.* **2016**, *6*, 18721. [[CrossRef](#)]
28. Feng, J.; Xiao, B. Effective Masses and Electronic and Optical Properties of Nontoxic MASnX<sub>3</sub> (X = Cl, Br, and I) Perovskite Structures As Solar Cell Absorber: A Theoretical Study Using HSE06. *J. Phys. Chem. C* **2014**, *118*, 19655–19660. [[CrossRef](#)]
29. Hsu, H.-Y.; Ji, L.; Du, M.; Zhao, J.; Yu, E.T.; Bard, A.J. Optimization of Lead-Free Organic–inorganic Tin(II) Halide Perovskite Semiconductors by Scanning Electrochemical Microscopy. *Electrochim. Acta* **2016**, *220*, 205–210. [[CrossRef](#)]
30. Cao, G. Lead-Free Organic-Inorganic Halide Perovskites Grown With Nontoxic Solvents. *Sci. Bull.* **2017**, *62*, 901–902. [[CrossRef](#)]
31. Bi, Z.; Rodríguez-Martínez, X.; Aranda, C.; Pascual-San-José, E.; Goñi, A.R.; Campoy-Quiles, M.; Xu, X.; Guerrero, A. Defect Tolerant Perovskite Solar Cells from Blade Coated Non-Toxic Solvents. *J. Mater. Chem. A* **2018**, *6*, 19085–19093. [[CrossRef](#)]
32. Ju, M.-G.; Chen, M.; Zhou, Y.; Garces, H.F.; Dai, J.; Ma, L.; Padture, N.P.; Zeng, X.C. Earth-Abundant Nontoxic Titanium(IV)-Based Vacancy-Ordered Double Perovskite Halides With Tunable 1.0 to 1.8 eV Bandgaps for Photovoltaic Applications. *ACS Energy Lett.* **2018**, *3*, 297–304. [[CrossRef](#)]
33. Xu, X.; Zhong, Y.; Shao, Z. Double Perovskites in Catalysis, Electrocatalysis, and Photo(electro)catalysis. *Trends Chem.* **2019**, *1*, 410–424. [[CrossRef](#)]
34. Slavney, A.H.; Hu, T.; Lindenberg, A.M.; Karunadasa, H.I. A Bismuth-Halide Double Perovskite With Long Carrier Recombination Lifetime for Photovoltaic Applications. *J. Am. Chem. Soc.* **2016**, *138*, 2138–2141. [[CrossRef](#)] [[PubMed](#)]
35. Zhou, L.; Xu, Y.-F.; Chen, B.-X.; Kuang, D.-B.; Su, C.-Y. Synthesis and Photocatalytic Application of Stable Lead-Free Cs<sub>2</sub>AgBiBr<sub>6</sub> Perovskite Nanocrystals. *Small* **2018**, *14*, e1703762. [[CrossRef](#)] [[PubMed](#)]
36. Chen, P.; Ong, W.; Shi, Z.; Zhao, X.; Li, N. Pb-Based Halide Perovskites: Recent Advances in Photo(electro)catalytic Applications and Looking Beyond. *Adv. Funct. Mater.* **2020**, *30*, 1909667. [[CrossRef](#)]
37. Greul, E.; Petrus, M.L.; Binek, A.; Docampo, P.; Bein, T. Highly Stable, Phase Pure Cs<sub>2</sub>AgBiBr<sub>6</sub> Double Perovskite Thin Films for Optoelectronic Applications. *J. Mater. Chem. A* **2017**, *5*, 19972–19981. [[CrossRef](#)]
38. Yang, J.; Zhang, P.; Wei, S.-H. Band Structure Engineering of Cs<sub>2</sub>AgBiBr<sub>6</sub> Perovskite through Order–Disordered Transition: A First-Principle Study. *J. Phys. Chem. Lett.* **2018**, *9*, 31–35. [[CrossRef](#)]
39. Xiao, Z.; Meng, W.; Wang, J.; Mitzi, D.B.; Yan, Y. Searching for Promising New Perovskite-Based Photovoltaic Absorbers: The Importance of Electronic Dimensionality. *Mater. Horiz.* **2016**, *4*, 206–216. [[CrossRef](#)]
40. Li, L. Probe for Electronic Dimensionality. *Nat. Phys.* **2010**, *6*, 7–8. [[CrossRef](#)]
41. Kresse, G.; Joubert, D. From Ultrasoft Pseudopotentials to the Projector Augmented-Wave Method. *Phys. Rev. B* **1999**, *59*, 1758–1775. [[CrossRef](#)]
42. Kresse, G.; Furthmüller, J. Efficiency of Ab-Initio Total Energy Calculations for Metals and Semiconductors Using a Plane-Wave Basis Set. *Comput. Mater. Sci.* **1996**, *6*, 15–50. [[CrossRef](#)]
43. Kresse, G.; Furthmüller, J. Efficient Iterative Schemes for Ab Initio Total-Energy Calculations Using a Plane-Wave Basis Set. *Phys. Rev. B* **1996**, *54*, 11169–11186. [[CrossRef](#)] [[PubMed](#)]
44. Engel, E.; Chevary, J.A.; Macdonald, L.D.; Vosko, S.H. Asymptotic Properties of the Exchange Energy Density and the Exchange Potential of Finite Systems: Relevance for Generalized Gradient Approximations. *Eur. Phys. J. D* **1992**, *23*, 7–14. [[CrossRef](#)]
45. Azofra, L.M.; Li, N.; Macfarlane, D.R.; Sun, C. Promising Prospects for 2D d<sub>2</sub>–d<sub>4</sub>M<sub>3</sub>C<sub>2</sub>transition Metal Carbides (MXenes) in N<sub>2</sub>capture and Conversion into Ammonia. *Energy Environ. Sci.* **2016**, *9*, 2545–2549. [[CrossRef](#)]
46. Li, T.; Zhao, X.; Yang, D.; Du, M.-H.; Zhang, L. Intrinsic Defect Properties in Halide Double Perovskites for Optoelectronic Applications. *Phys. Rev. Appl.* **2018**, *10*, 041001. [[CrossRef](#)]
47. Vasala, S.; Karppinen, M. A<sub>2</sub>B'B''O<sub>6</sub> Perovskites: A Review. *Prog. Solid State Chem.* **2015**, *43*, 1–36. [[CrossRef](#)]
48. Volonakis, G.; Filip, M.R.; Haghghirad, A.A.; Sakai, N.; Wenger, B.; Snaith, H.J.; Giustino, F. Lead-Free Halide Double Perovskites via Heterovalent Substitution of Noble Metals. *J. Phys. Chem. Lett.* **2016**, *7*, 1254–1259. [[CrossRef](#)]

49. Tang, C.; Chen, C.; Xu, W.; Xu, L. Design of Doped Cesium Lead Halide Perovskite as a Photo-Catalytic CO<sub>2</sub> Reduction Catalyst. *J. Mater. Chem. A* **2019**, *7*, 6911–6919. [[CrossRef](#)]
50. Zhao, X.-G.; Yang, D.; Ren, J.-C.; Sun, Y.; Xiao, Z.; Zhang, L. Rational Design of Halide Double Perovskites for Optoelectronic Applications. *Joule* **2018**, *2*, 1662–1673. [[CrossRef](#)]
51. McClure, E.T.; Ball, M.R.; Windl, W.; Woodward, P.M. Cs<sub>2</sub>AgBiX<sub>6</sub> (X = Br, Cl): New Visible Light Absorbing, Lead-Free Halide Perovskite Semiconductors. *Chem. Mater.* **2016**, *28*, 1348–1354. [[CrossRef](#)]
52. Meng, W.; Wang, X.; Xiao, Z.; Wang, J.; Mitzi, D.B.; Yan, Y. Parity-Forbidden Transitions and Their Impact on the Optical Absorption Properties of Lead-Free Metal Halide Perovskites and Double Perovskites. *J. Phys. Chem. Lett.* **2017**, *8*, 2999–3007. [[CrossRef](#)]
53. Xiao, Z.; Lei, H.; Zhang, X.; Zhou, Y.; Hosono, H.; Kamiya, T. Ligand-Hole in [SnI<sub>6</sub>] Unit and Origin of Band Gap in Photovoltaic Perovskite Variant Cs<sub>2</sub>SnI<sub>6</sub>. *Bull. Chem. Soc. Jpn.* **2015**, *88*, 1250–1255. [[CrossRef](#)]
54. Saparov, B.; Sun, J.-P.; Meng, W.; Xiao, Z.; Duan, H.-S.; Gunawan, O.; Shin, D.; Hill, I.G.; Yan, Y.; Mitzi, D.B. Thin-Film Deposition and Characterization of a Sn-Deficient Perovskite Derivative Cs<sub>2</sub>SnI<sub>6</sub>. *Chem. Mater.* **2016**, *28*, 2315–2322. [[CrossRef](#)]
55. Wang, M.; Zeng, P.; Wang, Z.; Liu, M. Vapor-Deposited Cs<sub>2</sub>AgBiCl<sub>6</sub> Double Perovskite Films Toward Highly Selective and Stable Ultraviolet Photodetector. *Adv. Sci.* **2020**, *7*, 1903662. [[CrossRef](#)]
56. Yang, X.; Chen, Y.; Liu, P.; Xiang, H.; Wang, W.; Ran, R.; Zhou, W.; Shao, Z. Simultaneous Power Conversion Efficiency and Stability Enhancement of Cs<sub>2</sub>AgBiBr<sub>6</sub> Lead-Free Inorganic Perovskite Solar Cell through Adopting a Multifunctional Dye Interlayer. *Adv. Funct. Mater.* **2020**, *30*, 2001557. [[CrossRef](#)]
57. Luo, J.; Li, S.; Wu, H.; Zhou, Y.; Li, Y.; Liu, J.; Li, J.; Li, K.; Yi, F.; Niu, G.; et al. Cs<sub>2</sub>AgInCl<sub>6</sub> Double Perovskite Single Crystals: Parity Forbidden Transitions and Their Application For Sensitive and Fast UV Photodetectors. *ACS Photon.* **2018**, *5*, 398–405. [[CrossRef](#)]
58. Liu, F.; Marongiu, D.; Pau, R.; Sarritzu, V.; Wang, Q.; Lai, S.; Lehmann, A.G.; Quochi, F.; Saba, M.; Mura, A.; et al. Ag/In Lead-Free Double Perovskites. *EcoMat* **2020**, *2*, e12017. [[CrossRef](#)]
59. Lee, B.; Stoumpos, C.C.; Zhou, N.J.; Hao, F.; Malliakas, C.; Yeh, C.Y.; Marks, T.J.; Kanatzidis, M.G.; Chang, R.P.H. Air-Stable Molecular Semiconducting Lodosalts for Solar Cell Applications: Cs<sub>2</sub>(SnI<sub>6</sub>) As a Hole Conductor. *J. Am. Chem. Soc.* **2014**, *136*, 15379–15385. [[CrossRef](#)]
60. Wang, A.; Yan, X.; Zhang, M.; Sun, S.; Yang, M.; Shen, W.; Pan, X.; Wang, P.; Deng, Z. Controlled Synthesis of Lead-Free and Stable Perovskite Derivative Cs<sub>2</sub>SnI<sub>6</sub> Nanocrystals via a Facile Hot-Injection Process. *Chem. Mater.* **2016**, *28*, 8132–8140. [[CrossRef](#)]
61. Chen, M.; Ju, M.-G.; Carl, A.D.; Zong, Y.; Grimm, R.L.; Gu, J.; Zeng, X.C.; Zhou, Y.; Padture, N.P. Cesium Titanium(IV) Bromide Thin Films Based Stable Lead-Free Perovskite Solar Cells. *Joule* **2018**, *2*, 558–570. [[CrossRef](#)]
62. Gou, G.; Young, J.; Liu, X.; Rondinelli, J.M. Interplay of Cation Ordering and Ferroelectricity in Perovskite Tin Iodides: Designing a Polar Halide Perovskite for Photovoltaic Applications. *Inorg. Chem.* **2016**, *56*, 26–32. [[CrossRef](#)] [[PubMed](#)]
63. Wei, F.; Deng, Z.; Sun, S.; Zhang, F.; Evans, D.M.; Kieslich, G.; Tominaka, S.; Carpenter, M.A.; Zhang, J.; Bristowe, P.D.; et al. Synthesis and Properties of a Lead-Free Hybrid Double Perovskite: (CH<sub>3</sub>NH<sub>3</sub>)<sub>2</sub>AgBiBr<sub>6</sub>. *Chem. Mater.* **2017**, *29*, 1089–1094. [[CrossRef](#)]
64. Wei, F.; Deng, Z.; Sun, S.; Xie, F.; Kieslich, G.; Evans, D.M.; Carpenter, M.A.; Bristowe, P.D.; Cheetham, A.K. The Synthesis, Structure and Electronic Properties of a Lead-Free Hybrid inorganic–organic Double Perovskite (MA)<sub>2</sub>KBiCl<sub>6</sub> (MA = Methylammonium). *Mater. Horiz.* **2016**, *3*, 328–332. [[CrossRef](#)]
65. Haruyama, J.; Sodeyama, K.; Han, L.; Tateyama, Y. Termination Dependence of Tetragonal CH<sub>3</sub>NH<sub>3</sub>PbI<sub>3</sub> Surfaces for Perovskite Solar Cells. *J. Phys. Chem. Lett.* **2014**, *5*, 2903–2909. [[CrossRef](#)]
66. Volonakis, G.; Giustino, F. Ferroelectric Graphene–Perovskite Interfaces. *J. Phys. Chem. Lett.* **2015**, *6*, 2496–2502. [[CrossRef](#)]
67. Volonakis, G.; Giustino, F. Surface Properties of Lead-Free Halide Double Perovskites: Possible Visible-Light Photo-Catalysts for Water Splitting. *Appl. Phys. Lett.* **2018**, *112*, 243901. [[CrossRef](#)]
68. Živković, A.; Somers, M.; Camprubi, E.; King, H.; Wolthers, M.; de Leeuw, N. Changes in CO<sub>2</sub> Adsorption Affinity Related to Ni Doping in FeS Surfaces: A DFT-D3 Study. *Catalysts* **2021**, *11*, 486. [[CrossRef](#)]
69. Xie, C.; Zhu, B.; Sun, Y.; Song, W.; Xu, M. Effect of Doping Cr on NH<sub>3</sub> Adsorption and NO Oxidation over the Fe<sub>x</sub>O<sub>y</sub>/AC Surface: A DFT-D Study. *J. Hazard. Mater.* **2021**, *416*, 125798. [[CrossRef](#)]
70. Ortiz-Medina, J.; Wang, Z.; Cruz-Silva, R.; Morelos-Gomez, A.; Wang, F.; Yao, X.; Terrones, M.; Endo, M. Defect Engineering and Surface Functionalization of Nanocarbons for Metal-Free Catalysis. *Adv. Mater.* **2019**, *31*, e1805717. [[CrossRef](#)]
71. Wang, S.; Jin, S.; Yang, S.; Chen, S.; Song, Y.; Zhang, J.; Zhu, M. Total Structure Determination of Surface Doping Nanocluster and Its Structure-Related Catalytic Property. *Sci. Adv.* **2015**, *1*, e1500441. [[CrossRef](#)]
72. Mansor, M.; Winkler, C.; Hochella, M.F.J.; Xu, J. Nanoparticulate Nickel-Hosting Phases in Sulfidic Environments: Effects of Ferrous Iron and Bacterial Presence on Mineral Formation Mechanism and Solid-Phase Nickel Distribution. *Front. Earth Sci.* **2019**, *7*, 151. [[CrossRef](#)]
73. Brinck, S.T.; Zaccaria, F.; Infante, I. Defects in Lead Halide Perovskite Nanocrystals: Analogies and (Many) Differences with the Bulk. *ACS Energy Lett.* **2019**, *4*, 2739–2747. [[CrossRef](#)]
74. Emery, A.A.; Wolverton, C. High-Throughput DFT Calculations of Formation Energy, Stability and Oxygen Vacancy Formation Energy of ABO<sub>3</sub> Perovskites. *Sci. Data* **2017**, *4*, 170153. [[CrossRef](#)]



75. Curnan, M.T.; Kitchin, J.R. Effects of Concentration, Crystal Structure, Magnetism, and Electronic Structure Method on First-Principles Oxygen Vacancy Formation Energy Trends in Perovskites. *J. Phys. Chem. C* **2014**, *118*, 28776–28790. [[CrossRef](#)]
76. Gergen, B.; Nienhaus, H.; Weinberg, W.H.; McFarland, E.W. Chemically Induced Electronic Excitations at Metal Surfaces. *Science* **2001**, *294*, 2521–2523. [[CrossRef](#)]
77. Foster, A.S.; Gejo, F.L.; Shluger, A.L.; Nieminen, R.M. Vacancy and Interstitial Defects in Hafnia. *Phys. Rev. B* **2002**, *65*, 174117. [[CrossRef](#)]
78. Dong, C.; Fu, J.; Liu, H.; Ling, T.; Yang, J.; Qiao, S.Z.; Du, X.-W. Tuning the Selectivity and Activity of Au Catalysts for Carbon Dioxide Electroreduction via Grain Boundary Engineering: A DFT Study. *J. Mater. Chem. A* **2017**, *5*, 7184–7190. [[CrossRef](#)]
79. Wang, Y.; Tian, Y.; Yan, L.; Su, Z. DFT Study on Sulfur-Doped G-C<sub>3</sub>N<sub>4</sub> Nanosheets as a Photocatalyst for CO<sub>2</sub> Reduction Reaction. *J. Phys. Chem. C* **2018**, *122*, 7712–7719. [[CrossRef](#)]
80. Chrétien, S.; Metiu, H. DFT Study of the Electronic Properties of LaOCl Surfaces. *J. Phys. Chem. C* **2011**, *116*, 681–691. [[CrossRef](#)]
81. Heydari, H.; Elahifard, M.; Behjatmanesh-Ardakani, R. Role of Oxygen Vacancy in the Adsorption and Dissociation of the Water Molecule on the Surfaces of Pure and Ni-Doped Rutile (110): A Periodic Full-Potential DFT Study. *Surf. Sci.* **2019**, *679*, 218–224. [[CrossRef](#)]
82. Zhao, S.; Gao, L.; Lan, C.; Pandey, S.S.; Hayase, S.; Ma, T. Oxygen Vacancy Formation and Migration in Double Perovskite Sr<sub>2</sub>CrMoO<sub>6</sub>: A First-Principles Study. *RSC Adv.* **2016**, *6*, 43034–43040. [[CrossRef](#)]
83. Liu, Y.; Palotas, K.; Yuan, X.; Hou, T.; Lin, H.; Li, Y.; Lee, S.-T. Atomistic Origins of Surface Defects in CH<sub>3</sub>NH<sub>3</sub>PbBr<sub>3</sub> Perovskite and Their Electronic Structures. *ACS Nano* **2017**, *11*, 2060–2065. [[CrossRef](#)] [[PubMed](#)]